

# Dual-fluid topology optimization of printed-circuit heat exchanger with low-pumping-power design

Geunhyeong Lee <sup>a,\*<sup>1</sup></sup>, Younghwan Joo <sup>b,1</sup>, Yonggyun Yu <sup>a</sup>, Hyun-Gil Kim <sup>a</sup>

<sup>a</sup> Korea Atomic Energy Research Institute, 111, Daedeok-daero 989 beon-gil, Yuseong-gu, Daejeon, 34057, Republic of Korea

<sup>b</sup> Korea Institute of Energy Research, 152, Gajeong-ro, Yuseong-gu, Daejeon, 34129, Republic of Korea



## ARTICLE INFO

### Keywords:

Topology optimization  
Printed-circuit heat exchanger  
Dual fluid  
Heat transfer  
3D printing

## ABSTRACT

This study proposes a novel design for a printed-circuit heat exchanger (PCHE) using a dual-fluid topology optimization method. To account for the three-dimensional (3D) heat transfer phenomena using the two-dimensional (2D) computational domains, three distinct physical domains are defined: two design domains with density fields of hot and cold fluids, and a thermal conduction domain placed between both fluid fields. To account for the local heat transfer variation within a design domain, the local heat transfer coefficient is expressed using the density fields for the hot- and cold-fluid domains. Here, the design geometry had pillar-shaped fixed density values considering the metal 3D printing. Each flow region had a constant flow rate as the boundary condition with the constraint of the maximum pressure drop between the inlet and outlet. The total amount of the heat transferred between the hot and cold domains was maximized as an objective function. For the validation, the thermal performance of the topology-optimized PCHE was compared to that of a conventional PCHE. The topology-optimized PCHE showed a 66% higher heat transfer rate compared to the conventional PCHE under identical pumping-power conditions.

## Nomenclatures

$c_p$	Specific heat capacity at constant pressure [J/(kg • K)]
$d_z$	Channel thickness for the shallow approximation [m]
$f$	Darcy friction factor
$h$	Heat transfer coefficient [W/(m <sup>2</sup> • K)]
$I$	Identity matrix
$k_f$	Thermal conductivity [W/(m • K)]
$K$	Viscous stress tensor
$Nu$	Nusselt number
$p$	Penalty value
$p'$	Pressure [Pa]
$q$	Darcy penalization factor

\* Corresponding author.

E-mail address: [gh29@kaeri.re.kr](mailto:gh29@kaeri.re.kr) (G. Lee).

<sup>1</sup> Lee and Joo are co-first authors and equally contributed.

<https://doi.org/10.1016/j.csite.2023.103318>

Received 11 October 2022; Received in revised form 4 May 2023; Accepted 16 July 2023

Available online 17 July 2023

2214-157X/© 2023 The Authors. Published by Elsevier Ltd. This is an open access article under the CC BY-NC-ND license (<http://creativecommons.org/licenses/by-nc-nd/4.0/>).

$q'$	Flowrate [ $\text{m}^3/\text{s}$ ]
$Q$	Heat [W]
$R$	Filter radius
$T$	Temperature [K]
$u$	Velocity [ $\text{m}/\text{s}$ ]
$V_0$	Initial topology material density
$\alpha$	Inverse permeability [ $\text{Pa} \cdot \text{s}/\text{m}^2$ ]
$\beta$	projection slope
$\gamma$	Material density
$\theta_c$	Domain control variable
$\theta_f$	Filtered material volume factor
$\mu$	Dynamic viscosity [Pa $\cdot$ s]
$\rho$	Density [ $\text{kg}/\text{m}^3$ ]

## 1. Introduction

A printed-circuit heat exchanger (PCHE) is a type of heat exchanger that provides high heat transfer performance with a compact size. Owing to these characteristics, the PCHEs are widely used in power plants. Examples include coal-fired power plants [1], molten salt reactors [2], small modular reactors [3], sodium fast reactors [4], and solar tower power plants [5]. Generally, a PCHE has a large heat transfer area achieved by forming minichannels on plates, which considerably reduces the pressure. Thus, researchers have focused on developing a channel geometry to reduce the pressure drop while maximizing the heat transfer capability of the PCHE [6, 7]. The representative channel geometries of the PCHE are zigzag, S-shaped, and airfoil fins [7,8]. Saeed et al. [8] investigated the effect of the PCHE channel geometry on the system performance of the supercritical carbon dioxide Brayton cycle. They reported that a C-shaped channel provides a better system performance, whereas the zigzag channel minimizes the size of the heat exchanger. Yang et al. [7] experimentally studied a PCHE using rhombic fin geometry and found that the thermal performance of the rhombic fin geometry was equivalent to that of the zigzag fin geometry with a reduced pressure drop.

Owing to the difficulty in defining the optimal PCHE shape based on the heat exchanger geometry, the topology optimization was used to determine the optimal object value within the specified area. The results of the topology optimization cannot be used in industrial applications because of its complex design. However, owing to recent developments in 3D metal printing in recent years, topology optimization can now be applied to the design for additive manufacturing (DfAM). Metal 3D printing is divided into two main methods: the power bed fusion (PBF) and directed energy deposition (DED) methods. The complex design of the topology-optimized heat exchanger can be achieved using the PBF method, which involves selective sintering in metal powder.

Topology optimization can provide the maximum performance system with any shape in a given design space and has been applied to the design of heat transfer devices [9]. Matsumori et al. [10] optimized the topology of a heat exchanger through fluid-thermal interactions. Dede et al. [11] experimentally determined the optimized topology of a heat sink. However, the outcome did not achieve the maximum heat transfer at a specific flow rate. Further, the fluid flow properties were considered for the heat sink experiment. A considerable level of heat-exchange maximization was achieved in the topology-optimized case [12]. To reduce the computational cost, Haertel et al. [13] proposed a pseudo three-dimensional (3D) method that converts 3D shapes into two-dimensional (2D) analysis. The heat sink problem was solved using the thermally coupled method.

These studies provide insight into the optimal channel geometry for heat transfer devices operating with a single working fluid. Further, researchers have applied topology optimization to the design of a heat transfer device with two distinct working fluids. Papazoglou [14] first simulated a non-mixing multi-flow heat exchanger to optimize the thermal energy exchange between two fluids. Saviers [15] et al. optimized the 3D topology of the heat exchanger geometry and experimentally demonstrated a commercial heat exchanger. This heat exchanger can reduce the flow pressure drop while increasing the heat transfer. Høghøj et al. [16] used a density-based topology optimization to thicken the wall between two fluids. Feppon et al. [17,18] optimized the topology using the level-set method and a non-mixing constraint.

The techniques to separate the two distinct fluids with a minimum gap are powerful in 3D problems because there is no cross-sectional area between both fluids. Here, the heat-exchange performance is directly affected by the size of the channel. A smaller mesh design incurs a considerable computational cost but can achieve a higher heat-exchange performance. The 3D topology optimization problem has a considerable computational cost owing to its sensitivity analysis in every iteration. Further, without a DfAM, the topology-optimized shape cannot be manufactured using the 3D printing method. Considering the high computational cost of the 3D topology optimization with two distinct working fluids and other manufacturing limitations, practical heat exchanger designs with cost-effective approaches and the application of the DfAM are required to facilitate industrial applicability.

Lee et al. [19] attempted topology-optimized PCHE research with a simple one-line channel and 5 W of heat transfer while minimizing thermal resistance. After that, topology optimization of airfoil fin shape in PCHEs for nuclear micro reactor using artificial intelligence techniques by Guillen et al. [20] to maximize heat transfer and minimize pressure drop.

In this study, we propose a topology optimization method for designing the whole channel geometry of a PCHE with two distinct working fluids. Two design domains for hot and cold fluids and a thermal conduction plate domain are defined to apply the pseudo-3D method. Here, the 3D heat transfer effect is considered by coupling the three domains. The local density field is defined for each design

domain. The governing equations are defined using the solid isotropic material with penalization (SIMP) method. To couple the energy equations in the three domains, the penalized heat transfer coefficient is defined using two distinct local density values and the flow characteristics. The fixed topology constraint condition for additive manufacturing is provided to make available 3D metal printing. The proposed methods are applied to a PCHE design example with a conventional channel geometry to examine the thermal performance and flow characteristics of the topology-optimized PCHE.

## 2. Methods and materials

### 2.1. Problem definition

Fig. 1 shows a typical PCHE design and how the three domains for the pseudo-3D method are derived from the PCHE. A PCHE was manufactured by alternately placing hot and cold plates. For each plate, the fluid channels were formed based on the predetermined positions of the fluid inlet and outlet. When hot and cold fluids were supplied to the flow channels during the operation, the heat transferred from the hot fluid (design domain i) in Fig. 1) to the thermal conduction domain (design domain ii) in Fig. 1), located between the hot and cold fluids. Further, the heat transferred from the thermal conduction domain to the cold fluid (design domain iii) in Fig. 1). Two distinct 2D design domains (i and iii in Fig. 1) were considered for the topology optimization of the PCHE. The first is the design domain of the hot-fluid region. Herein, instead of the parallel channels for the conventional PCHE, the geometry of the hot-fluid channels is determined by the local density variable of the hot fluid ( $\gamma_{\text{hot}}$ ). The second is the design domain for the cold fluid, wherein the geometry of the cold-fluid channels is determined by the local density variable of the cold fluid ( $\gamma_{\text{cold}}$ ). Here, a region is considered a solid or fluid when the local density is zero or one, respectively. For the wall located between both design domains, only the conductive heat transfers along the direction normal to the planes of the 2D domains was considered with the estimation of the conductive thermal resistance.

For the hot- and cold-fluid regions, a fully developed laminar flow was assumed with the Darcy term for the penalization of the SIMP approach. The governing equation was formulated as follows:

$$\rho(\mathbf{u} \bullet \nabla)\mathbf{u} = \nabla \bullet [-p'\mathbf{I} + \mathbf{K}] - 12 \frac{\mu\mathbf{u}}{d_z^2} - \alpha\mathbf{u} \quad (1)$$

$$\rho\nabla \bullet \mathbf{u} = 0 \quad (2)$$

where  $\rho$ ,  $p'$ ,  $\mathbf{u}$ ,  $\mathbf{I}$ ,  $\mathbf{K}$ , and  $\mu$  are the density, pressure, velocity, identity matrix, viscous stress tensor, and dynamic viscosity of the fluid, respectively. Further,  $d_z$  and  $\alpha$  represent the channel thickness for the shallow channel approximation and inverse permeability, respectively, which is a spatial property of the porous media. The shallow channel was approximated because the channel geometry with the proposed 2D domains was manufactured by forming shallow channels on the thin metal plates and combining them into a PCHE [21].

The temperature fields of the flow domains were obtained using the following equation [22]:

$$\begin{cases} \rho c_p \mathbf{u} \bullet \nabla T - k_f \nabla^2 T = Q_{\text{source}} & \text{in the fluid domain} \\ k_s \nabla^2 T = Q_{\text{source}} & \text{in the solid domain} \end{cases} \quad (3)$$

For other penalized properties, the SIMP approach was applied to the interpolation function as follows:

$$k(\gamma) = (k_s - k_f)\gamma^p + k_f \quad (4)$$

Further, the heat transfer was calculated using the heat transfer coefficients ( $h_{\text{hot}}, h_{\text{cold}}$ ), as follows:

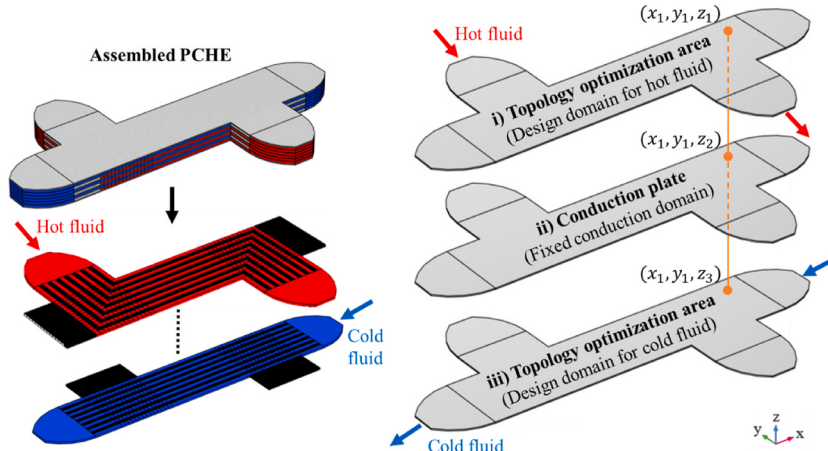


Fig. 1. Geometry of conventional PCHE and heat transfer coupling design domains for the pseudo-3D method.

$$Q_{source} = \begin{cases} \frac{h_{hot}}{d_z} (T_{hot} - T_{plate}) & \text{Hot fluid - Plate domain} \\ \frac{h_{cold}}{d_z} (T_{cold} - T_{plate}) & \text{Cold fluid - Plate domain} \end{cases} \quad (5)$$

where  $c_p$ ,  $T$ , and  $k_f$  represent the specific heat, temperature, and thermal conductivity of the fluid, respectively. The amount of heat exchange is expressed in  $Q_{source}$ . Although no mass transferred between the three domains, the heat transfer between these domains was closely coupled. Three locations share identical  $x$  and  $y$  coordinates along the  $z$ -direction, as shown in Fig. 1. Heat is transferred along the  $z$ -axis from the hot fluid to the plate region and from the cold fluid to the plate region. Here, the  $Q_{source}$  values were applied in all the three domains, including the hot-fluid, cold-fluid, and plate domains. In the case of the hot fluid-plate domain, heat was transferred from the hot fluid to the plate, whereas in that of the cold fluid-plate domain, heat was transferred from the plate to cold fluid. Thus, in the hot- and cold-fluid domains, the  $Q_{source}$  value is negative and positive, respectively.

The initial material density design is an important factor in topology optimization as it determines the final topological solid geometry. The initial design value was chosen as shown in Fig. 2(b) with conventional channel geometry to compare the difference with the conventional design one. The supporting design is required for 3D printing with metal. We locate the zero-density field that supports the 3D printing design in Fig. 2(a) in order to fix the supporting solid area.

In the design domain for the hot fluid, the fluid is supplied from the top-left corner and leaves the PCHE at the bottom-right corner. Thus, the hot fluid has an S-shaped overall flow path. In the design domain for the cold fluid, the inlet and outlet boundary conditions are placed on a similar axis. The overall flow direction does not change from the inlet to the outlet. In the hot- and cold-fluid regions, a constant inlet flow rate was assumed.

The boundary conditions are expressed as follow.

- Walls: (internal)  $u = 0$ ; (external)  $\frac{\partial T}{\partial n} = 0$ .
- Cold fluid: (inlet)  $q' = q'_{in}, T = T_{cold}$ ; (outlet)  $p' = 0$ .
- Hot fluid: (inlet)  $q' = q'_{in}, T = T_{hot}$ ; (outlet)  $p' = 0$ .
- Topology boundary:  $\gamma_{solid} = 0, \Delta p' \leq n \bullet p'_{ini}$ .

To perform the topology optimization, the physical properties of Eqs. (1)–(5) must be penalized with respect to the design variables ( $\gamma$ ). For the  $-\alpha u$  term that results in a zero-flow velocity in the solid phase ( $\gamma = 0$ ), Darcy penalization was used for  $\alpha$  as

$$\alpha = \alpha_{max} \frac{q(1 - \gamma)}{q + \gamma} \quad (6)$$

To compare the results of topology and original PCHE, the thermal-hydraulic performance factor (TPF) was employed. It is the ratio of the heat transfer improvement to a unit increase in pumping power, expressed as [23].

$$TPF = \frac{Nu_{top}/Nu_o}{(f_{top}/f_o)^{1/3}} \quad (7)$$

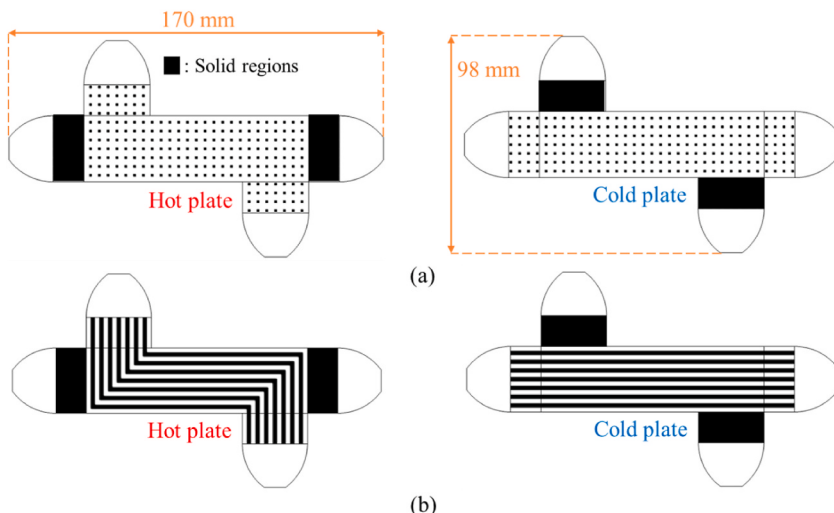


Fig. 2. Design domains for the pseudo-3D topology optimization of the PCHE: (a) boundary conditions and (b) initial topology material density geometries.

## 2.2. Optimization algorithm

The optimization problem was expressed as

$$\begin{aligned} \text{Maximize } Q_{\text{total}} &= \int_{\Omega_d} Q_{\text{source}} dV, \\ \text{s.t. } \int_{\Omega_d} \gamma dV &\leq V_0 \\ \Delta P_{\text{hot}} &< P_{0,\text{hot}} \\ \Delta P_{\text{cold}} &< P_{0,\text{cold}} \end{aligned} \quad (8)$$

where  $V_0$  is the mean initial topology material density of the PCHE and  $P_0$  the pressure drop of the initial topology channel geometry at the object flowrates. The globally convergent method of moving asymptotes (GCMMA) was used to determine the best layout of the topology results [24].

When the flow rate was used as a boundary condition in the absence of the pressure constraints, a solid region formed along the flow path. This resulted in the maximum heat transfer under conditions of the infinite pressure drop. Hence, a unique procedure was required to implement a constant inlet boundary condition. Here, we imposed constraints on the pressure drop in the hot- and cold-fluid domains. The values of the maximum pressure drop were determined based on the pressure drop for the conventional PCHE, as shown in Fig. 2(b).

Fig. 3 shows the flowchart of the optimization algorithm. The flow fields are obtained as the first step when the design domains and initial density fields are defined. Further, the energy equations are solved to obtain the temperature fields in the three domains. Here, the energy equations in these domains are coupled. Hence, inner iterations are performed until the thermal equilibrium is achieved for the design domains. If the velocity and temperature fields are obtained for a given density field, the design sensitivities are estimated using the field values.

The design sensitivity addresses the computation of the gradient of the objective as regards the changes in the topology. This gradient determines the direction of the topology ascent or descent for the object function maximization. Through the calculation of the sensitivity considering the pressure boundary constraints, the optimum topology that maximizes the heat transfer rate was determined. The adjoint sensitivity method was adopted owing to its advantage in application with numerous sensitivity parameters and few objective functions [25].

The size of the mesh was empirically determined to be 1/8 of the minimum flow channel to satisfy the computational cost and flow path generation problems. The intermediate gray region is an unphysical property region. Hence, this region must be minimized. A Helmholtz filter, which can impose a minimum length scale, was applied to reduce the gray region in the restricted mesh size. Here,  $\theta_f$ ,  $\theta_c$ , and  $R_{\min}$  denote the filtered material volume factor, domain control variable, and filter radius that imposes the minimum length scale, respectively.

$$\theta_f = R_{\min}^2 \nabla^2 \theta_f + \theta_c \quad (9)$$

The tangent hyperbolic projection was also applied to reduce the gray region, where  $\beta$  is the projection slope [26].

$$\gamma = \frac{\tanh(\beta(\theta_f - 0.5)) + \tanh(0.5\beta)}{\tanh(\beta(1 - 0.5)) + \tanh(0.5\beta)} \quad (10)$$

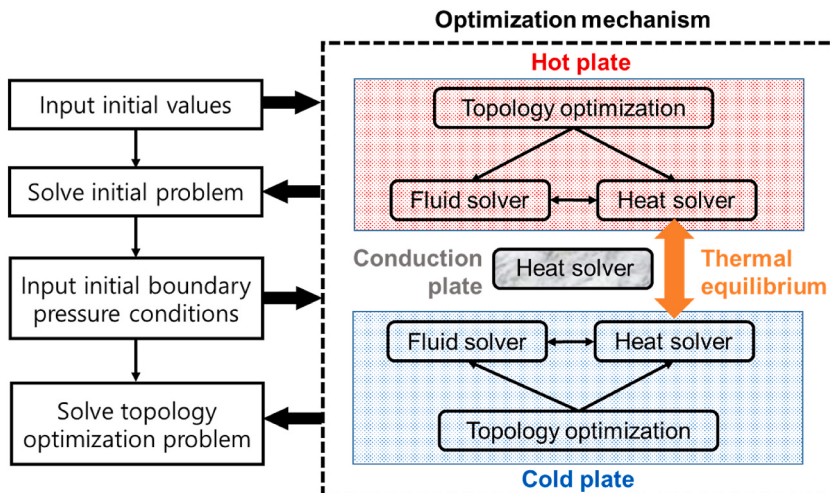


Fig. 3. Flow chart of the optimization algorithm.

The heat transfer efficiency was evaluated by dividing the heat transfer rate by the pumping power, as

$$\eta = \frac{Q_{\text{source}}}{\Delta P' q'} \quad (11)$$

where  $\Delta P$  and  $q'$  denote the pressure drop and flowrate, respectively.

**Table 1** presents the empirically chosen sweep parameters to determine the best converged values. The local minimum-topology optimization can be avoided if the sweep parameter is changed gradually [27]. The penalty value ( $p$ ) gradually increased to 4, which is the generally chosen value in the fluid topology problem. The  $q$  value for the Darcy penalization and  $\alpha_{\max}$  value were adopted as the reducing gray region while increasing the inverse permeability of the fluid.

In the simulation, the fluid and solid were set as water and stainless steel 316, respectively. The values of these properties are presented in **Table 2**. Temperature-independent properties were used to reduce computational costs. The temperature of the hot and cold fluids was set to 80 and 20 °C, respectively. The simulation was performed using COMSOL version 6.0.

### 3. Results and discussion

#### 3.1. Pseudo-3D topology optimization results

As the parameter sweep changed, the pseudo-3D topology was optimized when the flowrate was 0.03 Lpm, as shown in **Fig. 4**. This figure shows the design history of the pseudo-3D topology optimization with specified combinations of the sweep parameters. For this analysis, the flowrate was selected as 0.03 Lpm. The white and black regions represent the fluid and solid regions, respectively. Here, the topology density gradually changes based on the change in the sweep parameters. The heat transfer rate improved by 5.8% from 77.6 to 82.1 W compared to the initial topology value shown in **Fig. 2(b)**, which has an equal pressure drop and flowrate.

The velocity and temperature fields of the topology-optimized shapes are shown in **Fig. 5**. The inlet Reynolds number of the plates was 602, thereby portraying a laminar flow pattern. The maximum velocity was 77.8 mm/s, and the temperature differences between the inlet and outlet were 35.8 and 37.2 °C for the hot and cold plates, respectively. Different from the conventional PCHE in **Fig. 1**, the fluid channels were interconnected in the topology-optimized design. This enabled an increased mixing of the working fluids, which consequently resulted in the heat transfer enhancement. In the hot-fluid domain of the conventional PCHE, there exist corners wherein the working fluid experiences abrupt changes in the flow direction. This generally causes a large pressure drop. In the topology-optimized design, streamlined shapes were formed to adjust the flow direction while minimizing the flow resistance. In the cold-fluid domain, the topology-optimized channel induced an opposite cold-fluid flow direction relative to that of the hot fluid at the center.

The optimized designs were obtained at different flow conditions, that is, flowrate boundaries and pressure constraints. **Fig. 6** shows the pseudo-3D topology results with the flowrate conditions. The total heat transfer rate increased as the inlet flow rate increased. Compared to the conventional PCHE value, the heat transfer rate increased for all the cases under equal pressure drop and flowrate values. As the flow rate increased, the formation of the pin-fin array-like structures in topology optimization increased.

The topology-optimized designs were obtained by varying the maximum allowable pressure drop constraint, as shown in **Fig. 7**. From the reference value of the allowable pressure drop ( $P_0$ ), the maximum allowable pressure drop was determined as  $0.7P_0$  under a similar flow rate. When the maximum allowable pressure drop was relatively low, narrow channels were suppressed to satisfy the constraint. When the pressure constraint was  $0.7P_0$ , the channel geometry was close to a pin-fin array with a large channel width. To examine whether the optimized results can be considered as low-pumping-power designs, the resultant heat transfer rate was compared to that of a conventional PCHE with an equal pumping power. The heat transfer rate was increased by 9.9% when the pressure constraint was 0.7 times that of the initial pressure.

#### 3.2. 3D computational fluid dynamics (CFD) analysis results

The 2D topology optimized results with density fields provides the corresponding flow and temperature field with having gray elements and penalized properties at the solid boundaries. Therefore, the flow and heat transfer characteristics derived from the topology optimization may differ from the actual operating condition values. Thus, a simulation of the 3D analysis was conducted to validate the pseudo-3D results.

In the 2D analysis case, we only considered the heat transfer rate between each plate, but in the 3D analysis case, we created three hot and cold plates for each plate, enabling us to consider the heat transfer ability between all plates. COMSOL Multiphysics, version 6.0, was used to solve the CFD analysis. The convergence criterion for all variables is fixed at  $10^{-5}$ .

The #1–4 optimized result cases were determined by the constraint pressures of  $P = 1, 0.9, 0.8$ , and  $0.7P_0$ , as shown in **Fig. 8**. In the 3D geometry simulation, three cold- and hot-fluid plates each were used to form a computation domain for computational fluid

**Table 1**  
Simulated parameter sweep.

Parameter	Value		
Sweep #	1	2	3
$p$	2	3	4
$q$	0.1	1	1
$\alpha_{\max}$	$10^6$	$10^6$	$10^7$

**Table 2**  
Property values used for the simulation.

Property	Value	
	Solid (Stainless 316)	Liquid (water)
Density [ $\text{kg}/\text{m}^3$ ]	7960	988
Thermal conductivity [ $\text{W}/(\text{m} \cdot \text{K})$ ]	14.2	0.64
Specific heat [ $\text{J}/(\text{kg} \cdot \text{K})$ ]	465	4181
Dynamic viscosity [ $\text{Pa} \cdot \text{s}$ ]	–	$5.47 \cdot 10^{-4}$

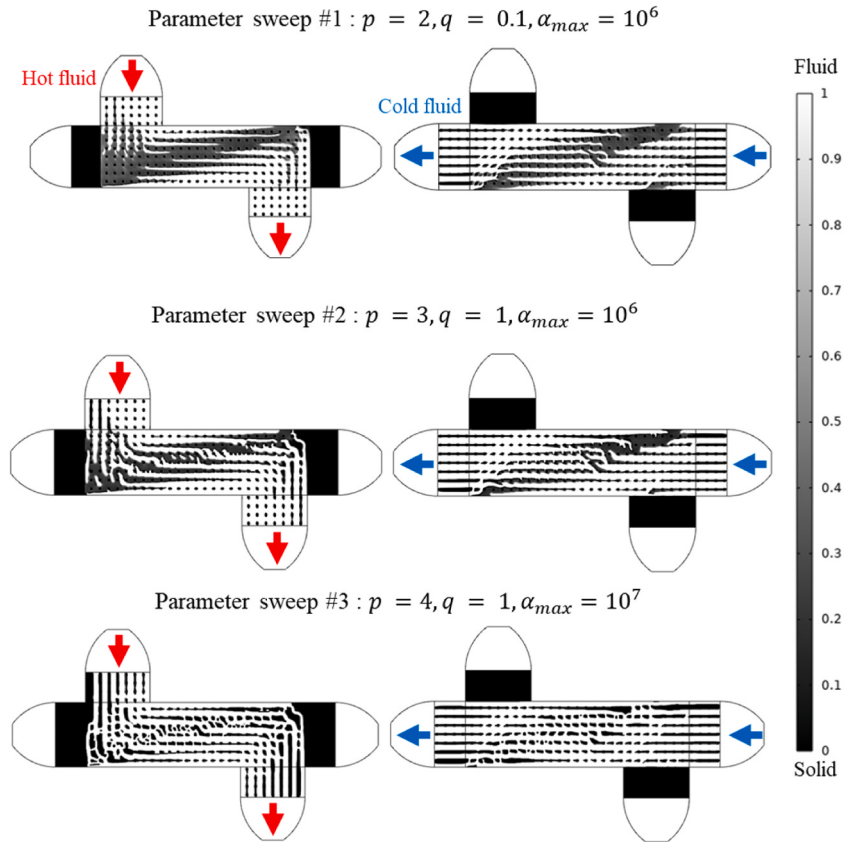


**Fig. 4.** Pseudo-3D topology optimization result based on the parameter sweeps when the flowrate condition is 0.03 Lpm.

dynamics (CFD) analysis.

The grid sensitivity was analyzed using the conventional PCHE results. As shown in Table 3, the composition of M3 mesh elements increased by 0.115% compared to that of M1 mesh elements. Fig. 8 shows the mesh structure of the M3 elements used for all of the 3D analysis, which was performed using M3 elements.

Considering the fluid properties, we analyzed the heat transfer rate results in terms of the fixed flow rate and pumping power. Table 4 presents the 3D conventional PCHE and topology-optimized # 1–4 results with a fixed flowrate of 0.03 Lpm. In the optimized result #4, the heat transfer rate based on the pumping power increased by 106%, and TPF was 1.27. In all the cases, the pressure drop rapidly reduced after the optimization, whereas all the heat transfer rates increased except for the optimized result #4.

The conventional PCHE results and topology-optimized results were analyzed under identical pumping power conditions. Fig. 9 shows the temperature difference of the topology-optimized heat exchanger. The increased heat transfer rate is represented in comparison with the conventional PCHE, which has the same pumping power as the topology-optimized one. In the optimized result #4, the heat transfer rate increased by 66% while maintaining an equal pumping power.

To validate our simulation results, we compared them to the experimental results of Seo et al. [28] for the case of a straight PCHE channel with fluid as water. Fig. 10 shows a good agreement between our simulation results and experimental results. The maximum variation was below 10%.

Fig. 11 shows a graphical comparison of the heat transferred as regards the pumping power. The average heat transfer rate increased by 32% at the same pumping power. The heat transfer rate relative to the pumping power ( $\eta$ ) is an important performance

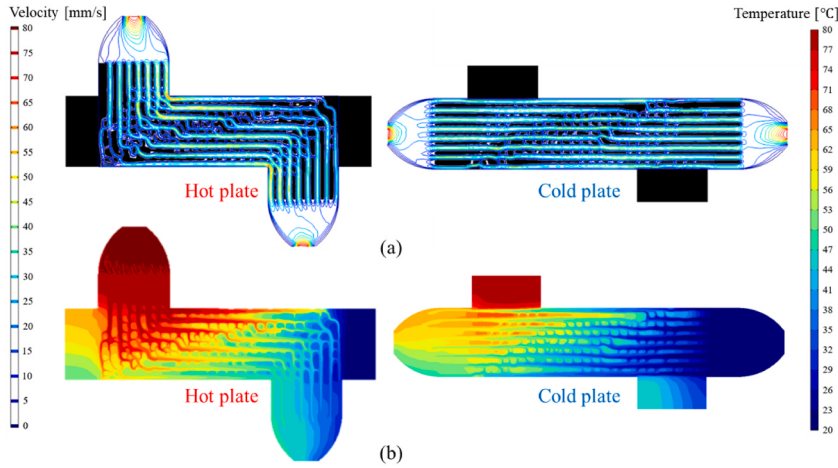


Fig. 5. Pseudo-3D topology-optimized results: (a) velocity and (b) temperature fields.

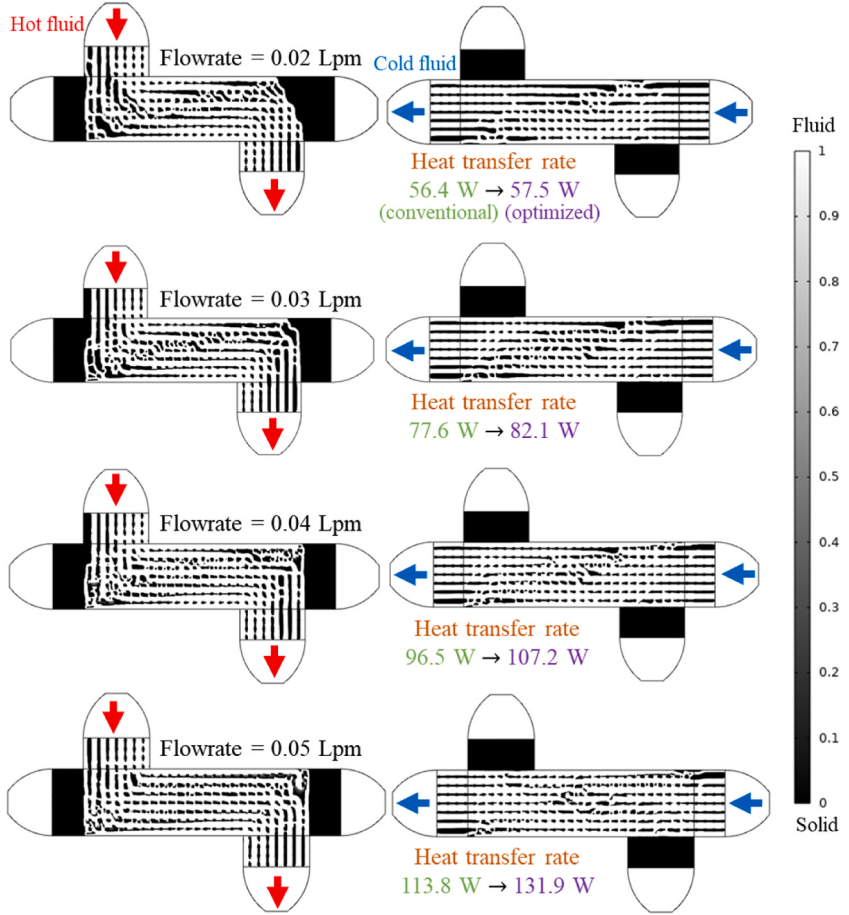


Fig. 6. Pseudo-3D topology results with the sweep parameter based on the flowrates.

index for designing efficient energy systems. In most power generation systems, heat exchangers account for a large amount of the system pressure drop. Hence, the pumping power for heat exchangers results in a loss of power generation for the entire system. As such, a lowered pumping-power requirement under a similar heat transfer performance enhances the power generation efficiency. Even with a high  $\eta$  value, the utility of the heat transfer device would be low if the heat transfer capacity is excessively small. As shown in Table 4, however, the high  $\eta$  values of the topology-optimized designs were primarily achieved through a low pumping power

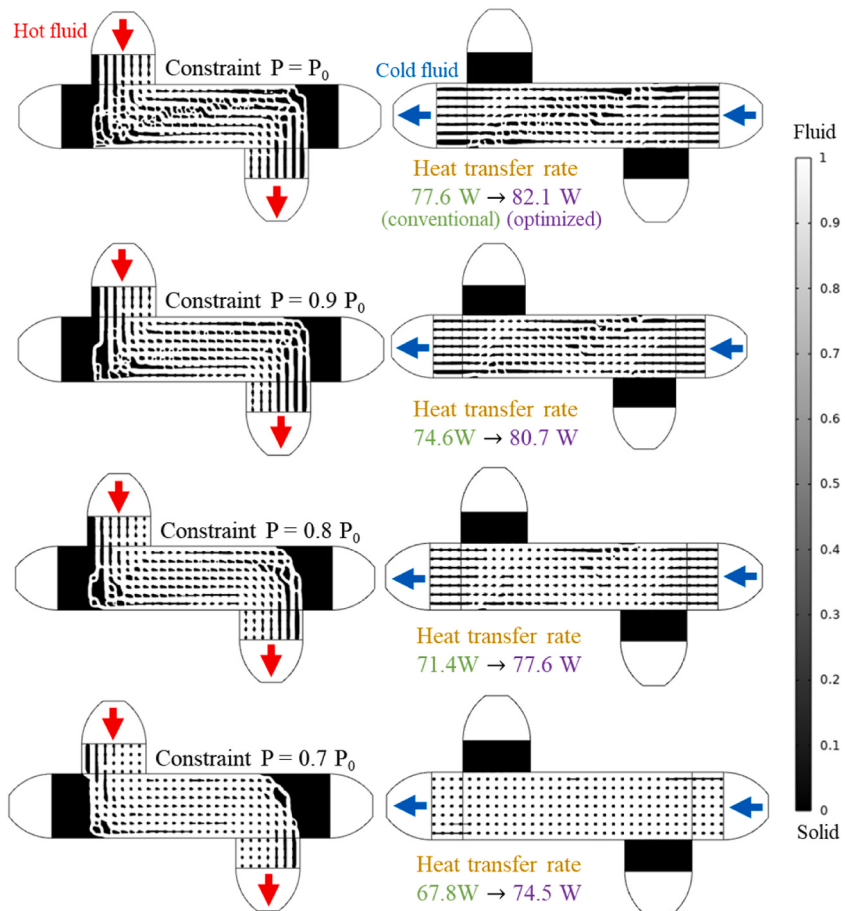


Fig. 7. Pseudo-3D topology results based on the constraint pressure conditions.

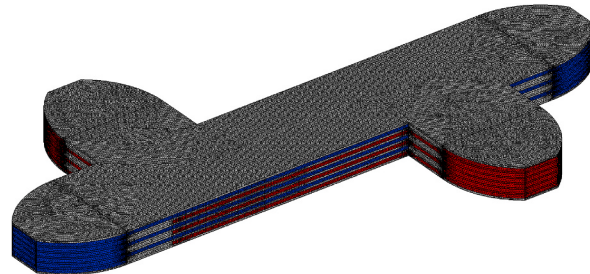


Fig. 8. Mesh structures of 3D-shaped PCHE.

Table 3

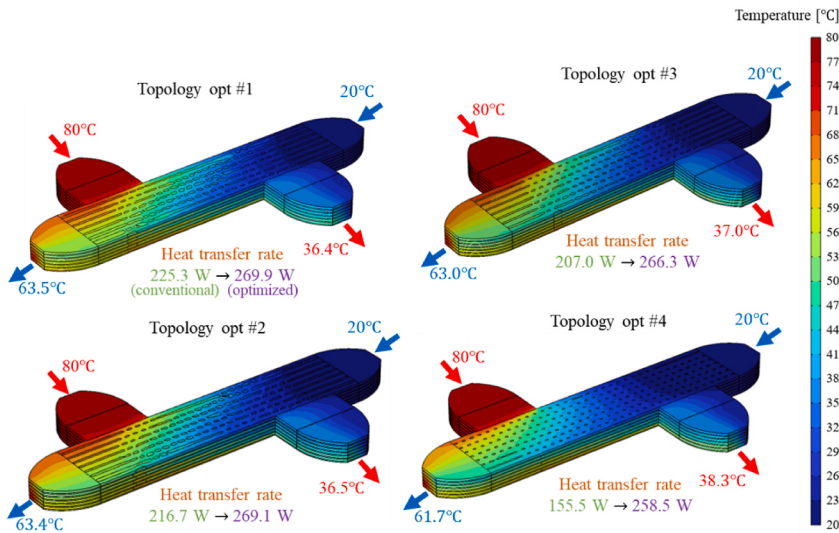
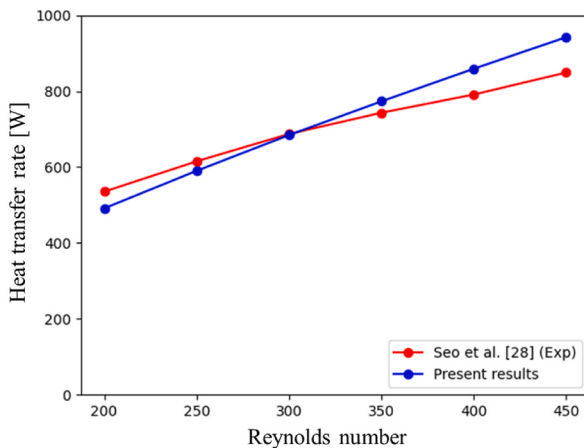
Grid sensitivity analysis for 3D geometry of conventional PCHE.

Elements number	Heat transfer rate [W]	Percentage error
M1 : 22,860,079	260.3	–
M2 : 16,957,261	259.9	0.154
M3 : 10,161,986	260.6	0.115
M4 : 7,075,501	258.5	0.692
M5 : 3,246,208	256.6	1.421

**Table 4**

3D topology result in the condition of a fixed flowrate of 0.03 Lpm.

	Conventional PCHE	Optimized result #1	Optimized result #2	Optimized result #3	Optimized result #4
Pressure drop [Pa]	83.9	58.2	52.6	46.7	40.4
Heat transfer rate [W]	260.6	269.9	269.1	266.3	258.5
Heat transfer rate/Pumping power	$2.07 \times 10^6$	$3.09 \times 10^6$ (+49.3%)	$3.41 \times 10^6$ (+64.7%)	$3.80 \times 10^6$ (+83.6%)	$4.27 \times 10^6$ (+106%)
Thermal-hydraulic performance factor (TPF)	–	1.17	1.21	1.24	1.27

**Fig. 9.** Topology-optimized 3D temperature results with constant pumping power.**Fig. 10.** Comparison between the results of the present numerical model and the experimental results of Seo et al. [28].

without compromising the heat transfer performance. Consequently, the topology-optimized PCHEs can be applied to systems wherein conventional PCHEs are used to enhance the efficiency of the system.

#### 4. Conclusion

In this study, the PCHE topology optimization was performed using the pseudo-3D method. Two design plates, cold and hot, were optimized using thermal equilibrium. A manufacturable topology optimization shape was derived by supporting the 3D printing using a zero-density constraint. By using different flow rates and differential pressure conditions, the topology-optimized shape showed

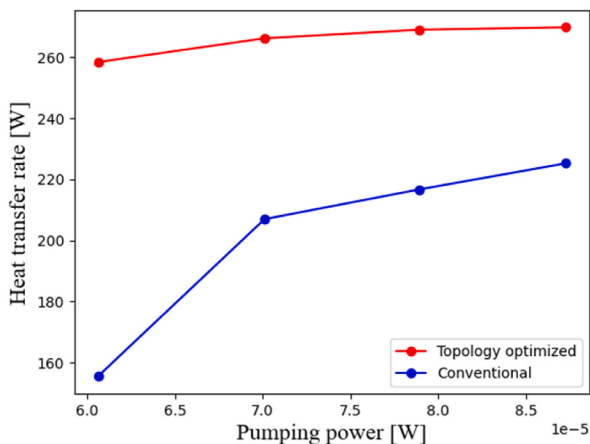


Fig. 11. Heat transfer rates based on to the pumping power.

improved results in terms of the heat exchange compared to the conventional PCHE. A 3D CFD analysis was performed to validate the topology-optimized results. The results of the CFD analysis revealed that the topology-optimized-shape heat exchanger increased the heat transfer rate by 66% in a specific case and 32% on average when compared to the conventional design with an equal pumping power.

The topology-optimized PCHEs were found to require a lower pumping power than the conventional PCHE while maintaining their heat transfer capacity. Such PCHEs can be applied to power generation systems wherein the conventional PCHEs are used to enhance the efficiency of the system. In future studies, a CFD-analyzed topology-optimized-shape heat exchanger will be manufactured using a metal 3D printer. It will be experimentally tested to prove that the heat transfer performance has improved compared to the conventional PCHE.

## Funding

This work was supported by the Korea Atomic Energy Research Institute (KAERI) R&D Programs [grant numbers KAERI-524490-23, KAERI-524450-23].

## Declaration of competing interest

The authors declare that they have no known competing financial interests or personal relationships that could have appeared to influence the work reported in this paper.

## Data availability

No data was used for the research described in the article.

## References

- [1] T. Ma, M.J. Li, J.L. Xu, F. Cao, Thermodynamic analysis and performance prediction on dynamic response characteristic of PCHE in 1000 MW S-CO<sub>2</sub> coal fired power plant, *Energy* 175 (2019) 123–138, <https://doi.org/10.1016/j.energy.2019.03.082>.
- [2] A. Di Ronco, A. Cammi, S. Lorenzi, Preliminary analysis and design of the heat exchangers for the molten salt fast reactor, *Nucl. Eng. Technol.* 52 (1) (2020) 51–58, <https://doi.org/10.1016/j.net.2019.07.013>.
- [3] C.W. Shin, H.C. No, Experimental study for pressure drop and flow instability of two-phase flow in the PCHE-type steam generator for SMRs, *Nucl. Eng. Des.* 318 (2017) 109–118, <https://doi.org/10.1016/j.nucengdes.2017.04.004>.
- [4] S.W. Lee, S.M. Shin, S. Chung, H. Jo, Evaluation of thermal-hydraulic performance and economics of printed circuit heat exchanger (PCHE) for recuperators of sodium-cooled fast reactors (SFRs) using CO<sub>2</sub> and N<sub>2</sub> as working fluids, *Nucl. Eng. Technol.* 54 (5) (2022) 1874–1889, <https://doi.org/10.1016/j.net.2021.11.023>.
- [5] K.Q. Chen, W.H. Pu, Q. Zhang, B.S. Lan, Z.Y. Song, Y.Q. Mao, Thermal performance analysis on steady-state and dynamic response characteristic in solar tower power plant based on supercritical carbon dioxide Brayton cycle, *Energy Sources, Part A Recovery, Util. Environ. Eff.* (2020), <https://doi.org/10.1080/15567036.2020.1838001>, 1–23.
- [6] Z. Rao, T. Xue, K. Huang, S. Liao, Multi-objective optimization of supercritical carbon dioxide recompression Brayton cycle considering printed circuit recuperator design, *Energy Convers. Manag.* 201 (2019), 112094, <https://doi.org/10.1016/j.enconman.2019.112094>.
- [7] Y. Yang, H. Li, B. Xie, L. Zhang, Y. Zhang, Experimental study of the flow and heat transfer performance of a PCHE with rhombic fin channels, *Energy Convers. Manag.* 254 (2022), 115137, <https://doi.org/10.1016/j.enconman.2021.115137>.
- [8] M. Saeed, A.S. Berrouk, M.S. Siddiqui, A.A. Awais, Effect of printed circuit heat exchanger's different designs on the performance of supercritical carbon dioxide Brayton cycle, *Appl. Therm. Eng.* 179 (2020), 115758, <https://doi.org/10.1016/j.applthermaleng.2020.115758>.
- [9] T. Dbouk, A review about the engineering design of optimal heat transfer systems using topology optimization, *Appl. Therm. Eng.* 112 (2017) 841–854, <https://doi.org/10.1016/j.applthermaleng.2016.10.134>.
- [10] T. Matsumori, T. Kondoh, A. Kawamoto, T. Nomura, Topology optimization for fluid–thermal interaction problems under constant input power, *Struct. Multidiscip. Optim.* 47 (4) (2013) 571–581, <https://doi.org/10.1007/s00158-013-0887-8>.

- [11] E.M. Dede, S.N. Joshi, F. Zhou, Topology optimization, additive layer manufacturing, and experimental testing of an air-cooled heat sink, *J. Mech. Des.* 137 (11) (2015), 111403, <https://doi.org/10.1115/1.4030989>.
- [12] H. Li, X. Ding, F. Meng, D. Jing, M. Xiong, Optimal design and thermal modelling for liquid-cooled heat sink based on multi-objective topology optimization: an experimental and numerical study, *Int. J. Heat Mass Tran.* 144 (2019), 118638, <https://doi.org/10.1016/j.ijheatmasstransfer.2019.118638>.
- [13] J.H.K. Haertel, K. Engelbrecht, B.S. Lazarov, O. Sigmund, Topology optimization of a pseudo 3D thermofluid heat sink model, *Int. J. Heat Mass Tran.* 121 (2018) 1073–1088, <https://doi.org/10.1016/j.ijheatmasstransfer.2018.01.078>.
- [14] P. Papazoglou, *Topology Optimization of Heat Exchangers*, [Master's thesis, Delft University of Technology, 2015].
- [15] K.R. Saviers, R. Ranjan, R. Mahmoudi, Design and validation of topology optimized heat exchangers, *AIAA Scitech (2019 Forum 2019)* 1465, <https://doi.org/10.2514/6.2019-1465>.
- [16] L.C. Höghoj, D.R. Nørhave, J. Alexandersen, O. Sigmund, C.S. Andreasen, Topology optimization of two fluid heat exchangers, *Int. J. Heat Mass Tran.* 163 (2020), 120543, <https://doi.org/10.1016/j.ijheatmasstransfer.2020.120543>.
- [17] F. Feppon, *Shape and Topology Optimization Applied to Compact Heat Exchangers*, 2021 hal-03207863.
- [18] F. Feppon, G. Allaire, C. Dapogny, P. Jolivet, Body-fitted topology optimization of 2D and 3D fluid-to-fluid heat exchangers, *Comput. Methods Appl. Mech. Eng.* 376 (2021), 113638, <https://doi.org/10.1016/j.cma.2020.113638>.
- [19] G. Lee, Y. Joo, H. Kim, Y. Yu, *The Analysis of Topology Optimized 3D Printing Heat Exchanger for the Small Nuclear Reactor*, KNS Autumn meeting, 2021, 2021.
- [20] D.P. Guillen, A.W. Abboud, J. Bennink, Topology optimization of an airfoil fin microchannel heat exchanger using artificial intelligence, *Nucl. Eng. Des.* 391 (2022), 111737, <https://doi.org/10.1016/j.nucengdes.2022.111737>.
- [21] A.B. Comsol, *CFD Module User's Guide, COMSOL Multiphysics® v. 6.0, Stockholm, Sweden*, 2021, pp. 73–74.
- [22] K. Ghachem, W. Aich, L. Kolsi, Computational analysis of hybrid nanofluid enhanced heat transfer in cross flow micro heat exchanger with rectangular wavy channels, *Case Stud. Therm. Eng.* 24 (2021), 100822, <https://doi.org/10.1016/j.csite.2020.100822>.
- [23] M. Omri, H. Smaoui, L. Frechette, L. Kolsi, A new microchannel heat exchanger configuration using CNT-nanofluid and allowing uniform temperature on the active wall, *Case Stud. Therm. Eng.* 32 (2022), 101866, <https://doi.org/10.1016/j.csite.2022.101866>.
- [24] K. Svanberg, *MMA and GCMMA-Two Methods for Nonlinear Optimization*, 2007. Technical Report.
- [25] Y. Cao, S. Li, L. Petzold, Adjoint sensitivity analysis for differential-algebraic equations: algorithms and software, *J. Comput. Appl. Math.* 149 (1) (2002) 171–191.
- [26] F. Wang, B.S. Lazarov, O. Sigmund, On projection methods, convergence and robust formulations in topology optimization, *Struct. Multidiscip. Optim.* 43 (6) (2011) 767–784, <https://doi.org/10.1007/s00158-010-0602-y>.
- [27] M.P. Bendsoe, O. Sigmund, Material interpolation schemes in topology optimization, *Arch. Appl. Mech.* 69 (9) (1999) 635–654, <https://doi.org/10.1007/s004190050248>.
- [28] J.W. Seo, Y.H. Kim, D. Kim, Y.D. Choi, K.J. Lee, Heat transfer and pressure drop characteristics in straight microchannel of printed circuit heat exchangers, *Entropy* 17 (5) (2015) 3438–3457, <https://doi.org/10.3390/e17053438>.